

Determining the Cramer-Rao Lower Bound in Magnetic Resonance Imaging

Purpose

Often when observing and processing medical images it is desired to minimize the noise in the images and increase the signal, which leads to a higher signal to noise ratio (SNR) and potentially superior detection of pathology. In magnetic resonance (MR) imaging experiments where it is of interest to detect changes in tissue parameters locally, maximizing for SNR alone will not necessarily give the best result, as contrast to noise ratio (CNR) must also be taken into consideration. Whether the goal is to optimize for SNR or CNR, minimizing the variance (or mean square error) of the image data becomes the central goal.

There are several imperfections in modern MR scanners, such as: 1) non-uniform static magnetic field (B_0 inhomogeneity) [1], 2) non-uniform excitation pulse (B_1 inhomogeneity) [2], 3) non-uniform sensitivity profile of the receiver coils [3], 4) non-linearity of the gradient fields used for spatial localization (gradient warping) [4], 5) quantization effects [5], and 6) correlated noise [6]. Extensive studies have been undertaken in order to find correction schemes for these imperfections, and have led to changes in the way that images are reconstructed from the acquired k -space data. All of these aspects change the propagation of uncertainty (*i.e.*, noise) from the acquired data to the estimated (or reconstructed) image.

The Cramer-Rao Lower Bound (CRLB) can be used to determine the minimum achievable variance of estimation parameters from measurements, assuming that the noise is unbiased (*i.e.*, the best solution in the minimum variance unbiased (MVU) estimator sense) [7]. The CRLB is a theoretical bound that cannot be improved upon if the estimate is unbiased. When Gaussian noise is used as part of a signal model, the CRLB can often be determined analytically and easily validated by simulations. MR imaging technologies involve complicated system models, particularly spatial signal models. The signal model itself becomes a function of the biological sample, and therefore determining the CRLB is experiment specific. CRLB optimization has been used for improving several MR imaging experiments [8,9], but the analysis is often limited to a single experimental type.

It is our overall hypothesis that the CRLB can be improved upon, under certain conditions, with non-linear reconstruction processing such as compressed sensing (CS), generalized autocalibrating partially parallel acquisitions (GRAPPA), or sensitivity encoding (SENSE) that are biased approaches. Some of these methods are commonly used to accelerate MR imaging in clinical protocols. When to use these non-linear methods is often determined with a

trial-and-error approach (*i.e.*, what method works best?), but by defining the CRLB, we could be lead to a realization of the quantitative parameters under which switching from conventional fast Fourier transform-based (FFT) reconstruction to one of the more sophisticated approaches is justified.

Here, we explain a generalized model for assessing the theoretical CRLB of the MR acquisition channel. Simulations using a digital brain phantom are performed to demonstrate the accuracy of this derivation, and then, the simulations are modified to show how the previously described MR system imperfections change the CRLB.

Methods

MR Signal Model

The signal model was constructed from brain anatomy images provided by the Montreal Neurological Institute [10]. Data was acquired at 1 mm^3 isotropic resolution and was of size $181 \times 217 \times 181$ and was padded with zeros to $256 \times 256 \times 192$. Data was segmented into ten separate tissue categories: 1) background, 2) cerebral spinal fluid (CSF), 3) gray matter (GM), 4) white matter (WM), 5) fat, 6) muscle/skin, 7) skin, 8) skull, 9) glial matter, and 10) connective tissue. MR parameters at 3 T were assigned to the each tissue type with values as per Table 1.

Table 1: MR properties used for each tissue type at 3 T.

Tissue Type	T_2 , [ms]	T_1 [ms]	M_0	Freq Shift [Hz]
Background	0	0	0	0
CSF	2200	4500	1.00	0
GM	100	1140	0.80	0
WM	80	800	0.65	0
Fat	60	290	0.90	-440
Muscle/Skin	50	1080	1.00	0
Skin	50	1080	1.00	0
Skull	0	0	0	0
Glial Matter	100	1140	0.80	0
Connective	50	1080	1.00	0

Non-uniformity of the B_0 and B_1 fields were simulated for the data volume using ranges that are observed with modern MR systems [11]. These fields were taken into consideration when the signal was calculated. Imperfections from coil sensitivity profiles were introduced using a Gaussian kernel centered outside the imaged volume and, placed around the imaged volume in a typical birdcage coil configuration [12].

Two separate signal equations were used to calculate MR signal from the assigned parameters, however other signal equations could be substituted depending on the application pulse sequence. The two pulse sequences simulated in this study were spin echo (SE) and spoiled gradient recalled echo sequences (SPGR).

$$\text{SE: } s = M_0 \left(1 - 2e^{-((TR-TE)/2)/T1} - e^{-TR/T1} \right) e^{-TE/T2} \quad [1a]$$

$$\text{SPGR: } s = \frac{M_0 \left(1 - e^{-TR/T1} \right)}{1 - \cos(\alpha) e^{-TR/T1}} \sin(\alpha) e^{-TE/T2} \quad [1b]$$

The k -space signal model was then generated from the simulated image signal model for both pulse sequence types.

$$k(\bar{r}, m) = \text{FFT} \left[C \left[GW \left[S(\bar{r}) \right], m \right] \right], \quad [2]$$

where \bar{r} is the spatial position (*i.e.*, $[x, y, z]$), the operations, $\text{FFT}[\bullet]$, $GW[\bullet]$ and $C[\bullet]$ denote the Fourier transform operation, the gradient non-linearity operation computed with spherical harmonics [13], and the individual coil sensitivity profiles (one for each channel), respectively, and m represents the particular imaging coil. In these experiments a 32 channel system was simulated. $S(\bullet)$ is the MR signal calculated from Eq [1].

MR Imaging Channel Model

The MR channel model in complex; several correction schemes are performed during image reconstruction in order to improve image quality. However, for derivation purposes, we remove these imperfections from our equations to present a simplified and best-case scenario. The k -space signal model from Eq [2] is sampled using the well-established frequency-encoding equation, it is at this stage where noise is introduced with a complex circularly normal (CN) distribution, having a mean of zero and a covariance of $\sigma_k^2 Q$.

$$k(t_n, m) = \gamma \int_{t_0}^{t_n} G(\bar{r}) dt + CN(0, \sigma_k^2 Q), \quad [3]$$

where γ is a gyro-magnetic constant, and $G(\bullet)$ is the gradient-waveform function. In practical circumstances it is not always true that noise will have zero mean, however, in this model the noise is deterministic, and so, if there were a bias due to noise at this level it could be measured and removed. Furthermore, in practice the noise from different channels would be correlated, but for this best-case scenario we assume the noise is uncorrelated and that the Q matrix is diagonal.

Using the inverse FFT, and combining the coil images with a sum-of-squares operation, the image signal becomes a function of chi-squared distributed noise,

$$\hat{S}(\bar{r}) = S(\bar{r}) + \chi_M^2. \quad [4]$$

A central chi-squared distribution can be approximated as a normal distribution having a mean and a variance of $M\sigma_k^2$ and $2M\sigma_k^2$, respectively, where M is the number of summations. When the central chi-squared noise distribution is broken into its first and second moments, the signal estimation function becomes,

$$\hat{S}(\bar{r}) = S(\bar{r}) + E \left[N(\mu, \sigma_S^2) \right] + N(0, \sigma_S^2), \quad \text{and} \quad [5]$$

$$\hat{S}(\bar{r}) = S(\bar{r}) + \mu_S + N(0, \sigma_S^2). \quad [6]$$

The noise introduces a bias to each signal value. *A priori* knowledge of the noise introduced in k -space can lead to more accurate estimates of individual voxel signal estimations. A bias is introduced as the signal value uncertainty does not have zero mean, and thus, the estimated image becomes a function of the noise. If the k -space signal noise level is measured then this bias can be determined and removed.

Letting $\theta = \bar{S} + E[\bar{\mu}_S]$, then the likelihood function of the signal in a given pixel is defined by,

$$p(\bar{S}; \theta) = \frac{1}{(2\pi\sigma^2)^{N/2}} e^{-\frac{1}{2\sigma^2} (\bar{S} - \theta)^H (\bar{S} - \theta)}, \quad [7]$$

and then the score of the likelihood function is:

$$\frac{d \ln p(\bar{S}; \theta)}{d\theta} = -\sigma_S^2 (\bar{S} - \theta). \quad [8]$$

The CRLB and the Fisher information, are $1/\sigma_S^2$ and σ_S^2 , respectively. It should be noted that this expression is the classical formation of the CRLB [7].

Computer Simulation

Simulations were first performed in order to validate that the CRLB derivation was accurate. Using the brain k -space signal model, and without any distortions (from B_0 inhomogeneity, B_1 inhomogeneity, gradient warping, coil sensitivity and correlated noise), a Monte Carlo simulation was undertaken. The k -space signal model was sampled with known gradient trajectories inherent to the chosen sequences (SE: TR = 1500 ms, TE = 750 ms; and SPGR: TR = 3.4 ms and TE = 1.8 ms, flip = 10°). The cross correlation matrix, Q , was modeled as $q_{ij} = 1 - e^{a(j-i)}$, with $a=0.1$. All simulations in this study were performed with 1000 trials.

The distributions of the measured signals were recorded (to create histograms) along with the variance and mean deviation from the true signal values.

The signal model was then generated with distortion as described in the MR signal model section. Correction for each of these distortion effects were also performed during

the simulated reconstruction. Again the distribution of the measured signal, and difference from mean were recorded. It was expected that the SNR will be spatially dependant like some of the distortion effects, and for this reason brain maps with values of variance were calculated.

A numerical comparison was then performed between the undistorted and distorted simulations to investigate how closely the CRLB approximates the best-case scenario found in the derivation, given the described distortion effects and the respective corrections.

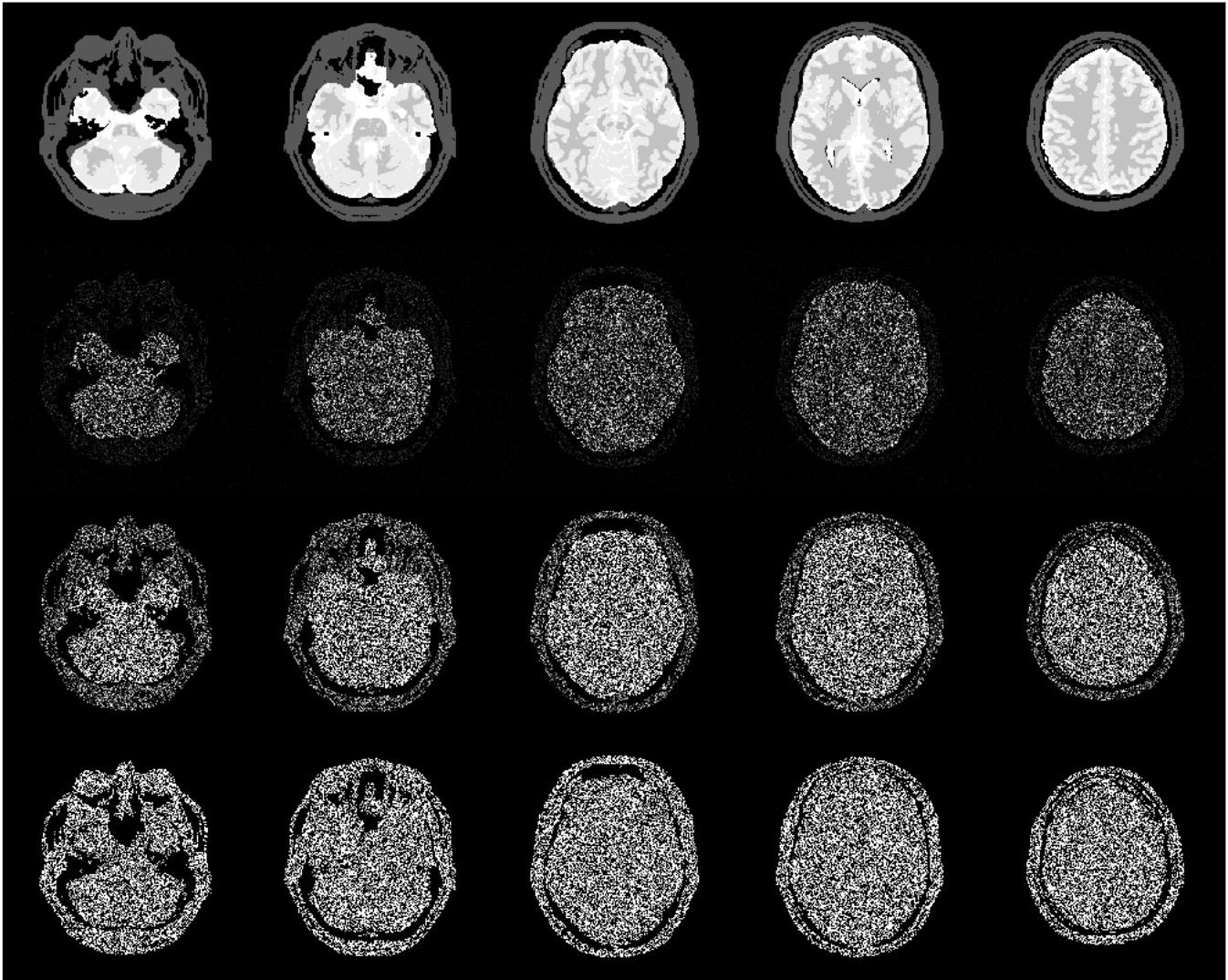


Figure 1: Each row has 5 images, representing the several spatial locations ($z = 35, 50, 65, 80, 120$) in the phantom. Slice thickness was 1 mm. The first row is the MR signal values calculated for the spin echo sequence, and can be used as a reference for the following rows. The second row is a map of the variance from the 'best case scenario' simulation (also using a spin echo technique). The third row contains variance maps, also using spin echo, but with the described non-uniformity and non-linearity effects. The fourth row is also a variance map, with distortions, but calculated with the SPGR sequence. Note: The second row required a multiplier of 10^3 in order to be visualized with row 3.

Results

We observed a factor of $>10^3$ in the CRLB between best-case scenario and non-uniform and non-linear case. Fig 1 depicts some of the results obtained in this simulation study. As expected (second row of Fig 1) there is a general uniformity across the images in the case where there is no spatial distortion, as we expected, each of the images had similar variance values across space and tissues. The measured variance values closely matched the

values calculated analytically using the derivation for several levels of k -space noise. The images did not show a purely uniform distribution of variance, we observed where the signal was lower, the variance did not always appear Gaussian, and thus the assumption used in the derivation that chi-squared noise would become Gaussian holds better in higher SNR cases. This finding closely matches reports in literature.

The third row of Fig 1 shows the variance maps across the brain for the SE sequence including distortion effects. The fourth row of Fig 1 shows the variance maps across the brain for the SPGR sequence including distortion.

Fig 2 shows histograms of a signal pixel of GM located at $z=50$, $x=100$, $y=100$ (the iso-centre is assumed at $z=96.5$, $x=128.5$, $y=128.5$). The two empirically derived probability mass functions indicate the improvement that could be observed by better correction of the distortions.

Discussion

This work is interesting as it demonstrates that, although MR systems have progressed extensively in the last 20 years, opportunity exists to improve the implementation with respect to minimizing image noise. We note, however, that it may not be realistic to actually meet the derived CRLB as optimizing to reduce one type of distortion may introduce another undesired effect.

As stated previously, it is our overall hypothesis that the CRLB can be improved upon with the images estimators that are biased. This work has demonstrated that we should not attempt to improve upon the theoretically derived CRLB, but rather use the values determined numerically that first take machine imprecision and other errors into account.

Acknowledgements

The authors would like to thank Dr A Janke (University of Queensland, Australia) for sharing his expertise with regard spherical harmonics and for providing his software to us. This generosity greatly helped with that section of the implementation for this study.

References

[1] Vovk U, Pernus F, Likar B. *A Review of Methods for Correction of Intensity Inhomogeneity in MRI*. IEEE Transactions in Medical Imaging. 2007. 3(26) p 405-421

[2] Zhang Z, Yip CY, Grissom W, Noll DC, Boada FE, Stenger VA. *Reduction of transmitter B_1 inhomogeneity with transmit SENSE slice-select pulses*. Magnetic Resonance in Medicine. 2007. 5(57) p 842-847

[3] Bydder M, Larkman DJ, Hajnal JV. *Combination of Signals from Array Coils using Image-Based Estimation of Coil Sensitivity Profiles*. Magnetic Resonance in Medicine. 2002. 3(47) p 539-548

[4] Doran SJ, Charles-Edwards L, Riensberg SA, Leach MO. *A Complete Distortion Correction for MR Images: I. Gradient Warp Correction*. Physics in Medicine and Biology. 2005. 50(7) p 1343-1362

[5] Gudbjartsson H., Samuel P. *The Rician Distribution of Noisy MRI Data*. Magnetic Resonance in Medicine. 1995. 6(34) p 910-914

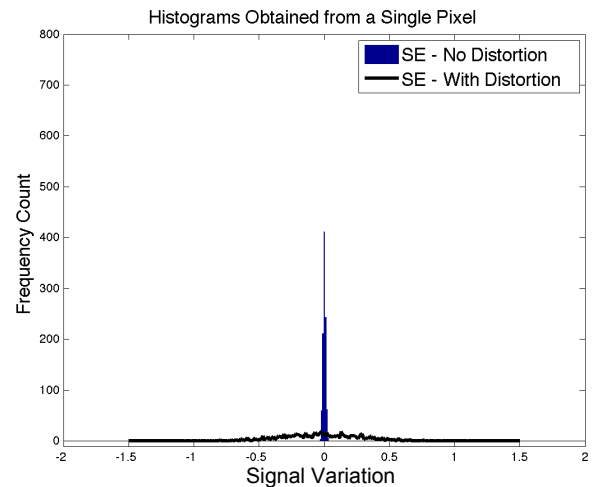


Figure 2: Histogram of the signal variance from a single pixel $z=50$, $x=100$, $y=100$. This figure visualizes the change in variance between the distorted and undistorted cases.

[6] Behin R, Bishop J, Henkelman RM. *Dynamic range requirements for MRI*. Concepts in Magnetic Resonance Part B: Magnetic Resonance Engineering. 2005. 1(26B) p 28-35

[7] Kay S. *Fundamentals of Statistical Signal Processing: Estimation Theory*. Prentice Hall. 1993

[8] Alexander DC. *A General Framework for Experimental Design in Diffusion MRI and its Application in Measuring Direct Tissue-Microstructure Features*. Magnetic Resonance in Medicine. 2008. 2(60) p 439-448

[9] Cercignani M, Alexander DC. *Optimal Acquisition Schemes for In Vivo Quantitative Magnetization Transfer MRI*. Magnetic Resonance in Medicine. 2006. 4(56) p 803-810

[10] Cocosco CA, Kollokian V, Kwan RKS, Pike GB, Evans AC. *BrainWeb: Online Interface to a 3D MRI Simulated Brain Database*. Proceedings of 3rd International Conference on Functional Mapping of the Human Brain, Copenhagen. 1997.

[11] Setsompop K, Wald LL, Alagappan V, Gagoski B, Hebrank F, Fontius U, Schmitt F, Adalsteinsson E. *Parallel RF Transmission with eight channels at 3T*. Magnetic Resonance in Medicine. 2006. 5(56) p 1163-1171

[12] de Zwart JA, Ledden PJ, van Gelderen P, Bodurka J, Chu R, Duyn JH. *Signal-to-Noise Ratio and Parallel Imaging Performance of a 16-Channel Receive-Only Brain Coil Array at 3.0 Tesla*. Magnetic Resonance in Medicine. 2004. 1(51) p 22-26

[13] Janke A, Zhao H, Cowin GJ, Galloway GJ, Dordrell DM. *Use of Spherical Harmonic Deconvolution Methods to Compensate for Nonlinear Gradient Effects on MRI Images*. Magnetic Resonance in Medicine. 2004. 1(52) p 115-122